

Learning Radio Environments by Differentiable Ray Tracing

Jakob Hoydis, Fayçal Aït Aoudia, Sebastian Cammerer, Florian Euchner, Merlin Nimier-David, Stephan ten Brink, and Alexander Keller

Abstract—Ray tracing (RT) is instrumental in 6G research in order to generate spatially-consistent and environment-specific channel impulse responses (CIRs). While acquiring accurate scene geometries is now relatively straightforward, determining material characteristics requires precise calibration using channel measurements. We therefore introduce a novel gradient-based calibration method, complemented by differentiable parametrizations of material properties, scattering and antenna patterns. Our method seamlessly integrates with differentiable ray tracers that enable the computation of derivatives of CIRs with respect to these parameters. Essentially, we approach field computation as a large computational graph wherein parameters are trainable akin to weights of a neural network (NN). We have validated our method using both synthetic data and real-world indoor channel measurements, employing a distributed multiple-input multiple-output (MIMO) channel sounder.

Index Terms—Radio propagation, differentiable ray tracing, calibration, machine learning, channel measurements

I. INTRODUCTION

Ray tracing (RT) is a mature technology capable of accurately predicting the propagation of electromagnetic waves in many scenarios of interest [1]. In contrast to the widely used geometry-based stochastic channel models, e.g., [2], RT is able to generate spatially consistent channel impulse responses (CIRs) for specific radio environments. This is a key requirement for many 6G research topics, such as integrated sensing and communications (ISAC) [3], multi-modal sensing [4], s (RIS) [5], radio-based localization [6], machine learning (ML)-based transceiver algorithms [7], as well as some use-cases of the 3GPP study-item on ML for the air interface [8]. RT is also considered an important building block of digital twin networks [9], [10].

Research on RT has seen a surge in interest due to ML’s potential to speed up and improve the accuracy of calculations [11], [12]. Several studies have applied neural networks (NNs) for improved path loss prediction [13], [14], [15], [16], while [17] explores NNs for modeling how rays interact with surfaces. The influence of ML and NNs is also

J. Hoydis and F. Aït Aoudia are with NVIDIA, France (email: {jhoydis, faitaoudia}@nvidia.com).

S. Cammerer and A. Keller are with NVIDIA, Germany (email: {scammerer, akeller}@nvidia.com).

M. Nimier-David is with NVIDIA, Switzerland (email: mnimier-david@nvidia.com).

F. Euchner and S. ten Brink are with the University of Stuttgart, Germany, (email: {euchner, tenbrink}@inue.uni-stuttgart.de) and acknowledge support by the German Federal Ministry of Education and Research (BMBF) within the project KOMSENS-6G (grant no. 16KISK113).

J. Hoydis, F. Aït Aoudia, and S. Cammerer acknowledge financial support from the European Union under Grant Agreement 101096379 (CENTRIC).

reshaping the field of computer vision, notably through neural rendering techniques such as neural radiance fields (NeRFs) [18]. Simultaneously, the interest in inverse rendering and differentiable ray tracing methods grows [19], [20], [21].

The accuracy of RT predictions is fundamentally reliant on two key elements: the scene geometry and the characteristics of the materials involved, e.g., their conductivity σ and relative permittivity ϵ_r . While scene geometries can nowadays be rather easily obtained with high precision [22], there is no automated and scalable solution to obtain material characteristics. Finding these is a process known as *calibration*.

There are essentially three different approaches to ray tracer calibration in the literature. The first consists in measuring the material characteristics of individual objects [23] of which a scene is composed. While this approach is the only option when the acquisition of channel measurements is difficult, it does not scale to large and complex scenes. It is also independent of the actual RT process and hence cannot compensate for any mismatches in the geometry or field computations.

The second approach tries to tune material parameters to fit aggregate statistics of rays, such as path loss or delay spread, to measurements. In [24], a simplified RT model based on angle-independent reflection and penetration losses is proposed which allows for a closed-form calibration solution. The authors of [25] use simulated annealing to optimize the relative permittivity and loss tangent for an ultra-wideband (UWB) system in an indoor scenario. The idea has been extended to account for diffuse reflections in [26] and used in [27] for the calibration of a high-speed railway scenario.

The third approach aims at extracting individual rays from measurements which can then be matched to the RT predictions. In [28], a sophisticated calibration effort of a commercial ray tracer against outdoor high-precision measurements at 28 GHz is described. The novelty with respect to (w.r.t.) prior work is the calibration on a per-ray basis rather than on aggregate statistics which allows for the object-specific calibration of diffuse scattering parameters. A key step in the process is the extraction of rays from measurements in the angle-delay domain using super-resolution techniques and matching them to the RT-based predictions. The same technique was applied in [29] to an indoor industrial scenario.

The aim of this paper is to introduce a novel fourth calibration method that leverages the automatic gradient computation capabilities of differentiable ray tracers like Sionna RT [30]. After a suitable parametrization of the material characteristics, antenna and scattering patterns, the field computation can be seen as a large computational graph, similar to an NN,

with measurement positions as inputs and the corresponding channel frequency responses (CFRs) as outputs. The trainable parameters of this graph can then be optimized w.r.t. any differentiable loss function of the outputs using the same gradient-based methods which have led to the success of deep NNs, e.g., [31]. However, in contrast to NNs, the calibrated model is fully explainable as each parameter has a precise physical meaning. One may therefore think of our calibration approach as a special kind of physics-informed [32] or model-based NN. It scales to very complex scenes and allows for learning of antenna and scattering patterns which is out of reach for existing methods. The dataset, 3D model of the scene, and source code to reproduce all results presented in this paper are provided in [33] and [34].

The rest of this paper is structured as follows. Section II discusses relevant background on RT. Section III describes different parametrizations of materials, antenna and scattering patterns, and introduces the loss function used for training. Section IV contains a description of experiments with synthetic and measured data. Section V concludes the paper.

Notations: Vectors and matrices are denoted by boldface letters. Unit vectors are represented by a hat symbol, e.g., $\hat{\mathbf{x}}$. In a global coordinate system (GCS) with Cartesian standard basis $(\hat{\mathbf{x}}, \hat{\mathbf{y}}, \hat{\mathbf{z}})$, we denote by $\hat{\mathbf{r}}(\theta, \varphi)$, $\hat{\boldsymbol{\theta}}(\theta, \varphi)$, and $\hat{\boldsymbol{\varphi}}(\theta, \varphi)$ the spherical unit vectors.

II. RAY TRACING BACKGROUND

This section explains how a CIR is obtained in the open-source differentiable ray tracer Sionna RT [30]. While most of this material can be found in well-known text books and tutorial papers, we have decided to reproduce it here so that the reader can clearly understand which parameters can be calibrated, how they impact the CIR, and why the latter is differentiable w.r.t. to them.

A. Channel impulse response (CIR)

The CFR $H(f)$ between a transmitter and receiver at carrier frequency f is computed as the sum of M propagation paths (e.g., [35, Eq. (8)]):

$$H(f) = \sum_{i=1}^M \frac{\lambda}{4\pi} \underbrace{\mathbf{C}_R(\theta_i^R, \varphi_i^R)^H \mathbf{T}_i(\mathbf{C}_T(\theta_i^T, \varphi_i^T))}_{\triangleq a_i} e^{-j2\pi f \tau_i} \quad (1)$$

where λ is the wavelength, $(\theta_i^T, \varphi_i^T)$ and $(\theta_i^R, \varphi_i^R)$ are the angles of departure (AoD) and angles of arrival (AoA) of the i th path with delay τ_i and transfer function $\mathbf{T}_i: \mathbb{C}^2 \mapsto \mathbb{C}^2$. $\mathbf{C}_T(\theta, \varphi) \in \mathbb{C}^2$ and $\mathbf{C}_R(\theta, \varphi) \in \mathbb{C}^2$ are the transmit- and receive-antenna patterns, respectively. All of these terms will be explained in detail later on. Each path can hence be described by a complex coefficient $a_i \in \mathbb{C}$ and delay τ_i .

For an ideal orthogonal frequency-division multiplexing (OFDM) system with N (even) subcarriers spread Δ_f apart, the channel is characterized by the discrete CFR $H[n]$:

$$H[n] = H(f + n\Delta_f), \quad n = -\frac{N}{2}, \dots, \frac{N}{2} - 1. \quad (2)$$

We denote by $W = N\Delta_f$ the bandwidth. The discrete complex baseband-equivalent CIR $h[\ell]$ is obtained from $H[n]$ via an N -point inverse discrete Fourier transform (IDFT), i.e.,

$$h[\ell] = \frac{1}{\sqrt{N}} \sum_{n=-\frac{N}{2}}^{\frac{N}{2}-1} H[n] e^{j\frac{2\pi}{N}n\ell}, \quad \ell = -\frac{N}{2}, \dots, \frac{N}{2} - 1. \quad (3)$$

The vector with elements $h[\ell]$ is denoted $\mathbf{h} \in \mathbb{C}^N$.

B. Modeling of antennas

Antennas are described by their complex antenna pattern $\mathbf{C}(\theta, \varphi) \in \mathbb{C}^2$ which consists of a vertical $\hat{\boldsymbol{\theta}}(\theta, \varphi)$ and horizontal $\hat{\boldsymbol{\varphi}}(\theta, \varphi)$ component:

$$\mathbf{C}(\theta, \varphi) = [C_{\theta}(\theta, \varphi) \quad C_{\varphi}(\theta, \varphi)]^T. \quad (4)$$

The directional antenna gain $G(\theta, \varphi)$ is then given by

$$G(\theta, \varphi) = \|\mathbf{C}(\theta, \varphi)\|^2 \quad (5)$$

which satisfies

$$\int_0^{2\pi} \int_0^{\pi} G(\theta, \varphi) \sin(\theta) d\theta d\varphi = 4\pi \eta_{\text{rad}} \quad (6)$$

where $\eta_{\text{rad}} \in [0, 1]$ is the radiation efficiency. One can define antenna patterns by their directional gain and polarization slant angle ζ , where $\zeta = 0$ and $\zeta = \pi/2$ correspond to vertical and horizontal polarization, respectively:

$$\mathbf{C}(\theta, \varphi) = [\cos(\zeta)\sqrt{G(\theta, \varphi)} \quad \sin(\zeta)\sqrt{G(\theta, \varphi)}]^T. \quad (7)$$

We have chosen this polarization model for its simplicity. Other models are proposed in the literature, e.g., [2, Sec. 7.3.2]. Closed-form expressions for the directional gain of different antennas can be found in [36] and [2, Table 7.3-1]. In Section III-A, we describe a parametric differentiable antenna pattern that can be used for gradient-based calibration.

C. Transfer function

A propagation path consists of a sequence of Q scattering events, such as specular and diffuse reflections, as well as diffraction. For each scattering process, one needs to compute a relationship between the incoming field at the current scattering point $\mathbf{s}_j \in \mathbb{R}^3$, for $j = 1, \dots, Q$, and the created far-field at the next scattering point \mathbf{s}_{j+1} , where \mathbf{s}_0 and \mathbf{s}_{Q+1} denote the position of the transmitter and receiver, respectively.

For every scattering process, the electrical field is represented in its local basis. Since the field is transversal, it can always be represented by two orthogonal components p and q . Let us denote by $\mathbf{E}_j^{\text{Out}}(\mathbf{s}_{j+1}) \in \mathbb{C}^2$ the vector of the two components of the outgoing field of the j th scattering process at the $j+1$ th scattering point, represented in the basis of the j th scattering process. The incoming field at the $j+1$ th scattering point in its own basis $\mathbf{E}_{j+1}^{\text{In}}(\mathbf{s}_{j+1})$ is then given by

$$\mathbf{E}_{j+1}^{\text{In}}(\mathbf{s}_{j+1}) = \mathbf{D}_{j+1} \mathbf{E}_j^{\text{Out}}(\mathbf{s}_{j+1}) \quad (8)$$

where

$$\mathbf{D}_{j+1} = \begin{bmatrix} (\hat{\mathbf{e}}_{p,j+1}^{\text{In}})^T & \hat{\mathbf{e}}_{p,j}^{\text{Out}} & (\hat{\mathbf{e}}_{p,j+1}^{\text{In}})^T & \hat{\mathbf{e}}_{q,j}^{\text{Out}} \\ (\hat{\mathbf{e}}_{q,j+1}^{\text{In}})^T & \hat{\mathbf{e}}_{p,j}^{\text{Out}} & (\hat{\mathbf{e}}_{q,j+1}^{\text{In}})^T & \hat{\mathbf{e}}_{q,j}^{\text{Out}} \end{bmatrix} \quad (9)$$

is a basis transformation matrix, and $(\hat{\mathbf{e}}_{p,j}^{\text{In}}, \hat{\mathbf{e}}_{q,j}^{\text{In}})$ and $(\hat{\mathbf{e}}_{p,j}^{\text{Out}}, \hat{\mathbf{e}}_{q,j}^{\text{Out}})$ are pairs of orthogonal basis vectors used for the description of the incoming and outgoing field of the j th scattering process, respectively.

The incoming and outgoing field of the j th scattering process are related as

$$\mathbf{E}_j^{\text{Out}}(\mathbf{s}_{j+1}) = \mathbf{F}_j(\mathbf{E}_j^{\text{In}}(\mathbf{s}_j)) \quad (10)$$

where $\mathbf{F}_j : \mathbb{C}^2 \mapsto \mathbb{C}^2$ depends on the type of scattering process as will be discussed below and, in particular, we have

$$\mathbf{E}_0^{\text{In}}(\mathbf{s}_0) = \mathbf{C}_T(\theta^T, \varphi^T) \quad (11)$$

$$\mathbf{F}_0(\mathbf{E}_0^{\text{In}}(\mathbf{s}_0)) = \frac{e^{-j2\frac{\pi}{\lambda}d_1}}{d_1} \mathbf{E}_0^{\text{In}}(\mathbf{s}_0) \quad (12)$$

where $d_j = \|\mathbf{s}_j - \mathbf{s}_{j-1}\|$ for $j = 1, \dots, Q+1$.

Combining (8)–(12), we arrive at the following expression for the relationship between the transmitted and received field

$$\mathbf{E}_{Q+1}^{\text{In}}(\mathbf{s}_{Q+1}) = \mathbf{D}_{Q+1} \mathbf{F}_Q(\dots \mathbf{D}_1 \mathbf{F}_0(\mathbf{E}_0^{\text{In}}(\mathbf{s}_0))) \quad (13)$$

$$= \mathbf{T}(\mathbf{C}_T(\theta^T, \varphi^T)) e^{-j2\pi f \tau} \quad (14)$$

where we have factored out an exponential term representing the phase shift caused by the total propagation delay $\tau = (\lambda f)^{-1} \sum_q d_q$. The last equation defines the transfer function \mathbf{T}_i in (1) for the considered propagation path. The structure of this sequence of computations resembles the computational graph of a feed-forward NN. As long as all functions \mathbf{F}_j are differentiable, so will be the final CFR.

D. Reflection

We distinguish between specular and diffuse reflections and denote by S^2 the fraction of the reflected energy that is diffusely scattered, where $S \in [0, 1]$ is the scattering coefficient [37]. Similarly, R^2 is the specularly reflected fraction of the reflected energy, where $R = \sqrt{1 - S^2}$. We consider materials that are uniform non-magnetic dielectrics with relative permeability $\mu_r = 1$. A material is described by four parameters, the conductivity $\sigma \geq 0$, the relative permittivity $\varepsilon_r \geq 1$, the scattering coefficient S , and the cross polarization discrimination (XPD) coefficient $K_x \in [0, 1]$. The latter determines how much energy is transferred into the orthogonal polarization direction after a diffuse reflection [38]. Each material has a scattering pattern f_s that describes, similar to an antenna pattern, the directivity of the scattered field. The complex relative permittivity η is defined as [39, Eq. (9b)]

$$\eta = \varepsilon_r - j \frac{\sigma}{\varepsilon_0 \omega} \quad (15)$$

where ε_0 is the vacuum permittivity and $\omega = 2\pi f$.

1) *Specular reflection*: For an incident wave in vacuum with direction $\hat{\mathbf{k}}_i$ incident on a surface with permittivity η and surface normal $\hat{\mathbf{n}}$, the field transformation (10) is given as

$$\mathbf{F}_j(\mathbf{E}_j^{\text{In}}(\mathbf{s}_j)) = \begin{bmatrix} Rr_{\perp} & 0 \\ 0 & Rr_{\parallel} \end{bmatrix} \mathbf{E}_j^{\text{In}}(\mathbf{s}_j) A^r(\mathbf{s}_{j+1}, \mathbf{s}_j) e^{-j2\frac{\pi}{\lambda}d_{j+1}} \quad (16)$$

where $A^r(\mathbf{s}_{j+1}, \mathbf{s}_j)$ is the spreading factor [40, Eq. (24)] that depends on the shape of the wavefront and r_{\perp} , r_{\parallel} are the Fresnel reflection coefficients [39, Eq. (37)]:

$$r_{\perp} = \frac{\cos(\theta_i) - \sqrt{\eta - \sin^2(\theta_i)}}{\cos(\theta_i) + \sqrt{\eta - \sin^2(\theta_i)}} \quad (17)$$

$$r_{\parallel} = \frac{\eta \cos(\theta_i) - \sqrt{\eta - \sin^2(\theta_i)}}{\eta \cos(\theta_i) + \sqrt{\eta - \sin^2(\theta_i)}} \quad (18)$$

where $\cos(\theta_i) = -\hat{\mathbf{k}}_i^T \hat{\mathbf{n}}$. The basis vectors used to compute \mathbf{D}_{j+1} can be found in [41, Eq. (3.3)–(3.8)]. The reflected ray has direction $\hat{\mathbf{k}}_r = \hat{\mathbf{k}}_i - 2(\hat{\mathbf{k}}_i^T \hat{\mathbf{n}})\hat{\mathbf{n}}$. It is obvious that (16) is differentiable w.r.t. to the parameters ε_r , σ , S , as well as the input $\mathbf{E}_j^{\text{In}}(\mathbf{s}_j)$.

2) *Diffuse reflection (scattering)*: We consider the model from [38] for which the field transformation (14) is given as

$$\mathbf{F}_j(\mathbf{E}_j^{\text{In}}(\mathbf{s}_j)) = \frac{\|\mathbf{E}_j^{\text{In}}(\mathbf{s}_j)\|}{d_{j+1}} \begin{bmatrix} \sqrt{1 - K_x} e^{j\chi_1} \\ \sqrt{K_x} e^{j\chi_2} \end{bmatrix} e^{-j2\frac{\pi}{\lambda}d_{j+1}} \quad (19)$$

$$\|\mathbf{E}_j^{\text{In}}(\mathbf{s}_j)\|^2 = \|\mathbf{E}_j^{\text{In}}(\mathbf{s}_j)\|^2 \cos(\theta_i) dA S^2 \Gamma^2 f_s(\hat{\mathbf{k}}_i, \hat{\mathbf{k}}_s, \hat{\mathbf{n}}) \quad (20)$$

where $\chi_1, \chi_2 \sim U[0, 2\pi)$ are random phase terms, $\hat{\mathbf{k}}_s$ is the direction of the scattered ray, dA is the size of a small area element, $f_s(\hat{\mathbf{k}}_i, \hat{\mathbf{k}}_s, \hat{\mathbf{n}})$ is the scattering pattern, and Γ is the fraction of the incoming power that is reflected, i.e.,

$$\Gamma = \left\| \begin{bmatrix} r_{\perp} & 0 \\ 0 & r_{\parallel} \end{bmatrix} \mathbf{E}_j^{\text{In}}(\mathbf{s}_j) \right\| \|\mathbf{E}_j^{\text{In}}(\mathbf{s}_j)\|^{-1}. \quad (21)$$

Under the backscattering lobe model from [37], the scattering pattern has the following form

$$f_s(\hat{\mathbf{k}}_i, \hat{\mathbf{k}}_s, \hat{\mathbf{n}}) = \frac{1}{F_{\alpha_r, \alpha_s}(\theta_i)} \times \left[\Lambda \left(\frac{1 + \hat{\mathbf{k}}_r^T \hat{\mathbf{k}}_s}{2} \right)^{\alpha_r} + (1 - \Lambda) \left(\frac{1 + \hat{\mathbf{k}}_i^T \hat{\mathbf{k}}_s}{2} \right)^{\alpha_s} \right] \quad (22)$$

where $F_{\alpha_r, \alpha_s}(\theta_i)$ normalizes the hemispherical integral of the pattern to one, $\alpha_r, \alpha_s \geq 1$ are integer parameters that control the lobe width, and $\Lambda \in [0, 1]$ determines the fraction of the scattered energy in the specular lobe. The basis transformation matrix \mathbf{D}_{j+1} ensures that energy transfer between both polarization directions is correctly applied. While (19) is differentiable in all material parameters ε_r , σ , S , K_x as well as Λ , this is not the case for α_r and α_s . In Section III-B, we will present a fully differentiable version of a scattering pattern with similar structure.

E. Diffraction

Diffraction is modeled according to the uniform theory of diffraction (UTD) by [42] (see [41] for an introduction) with the heuristic extension to finitely conducting wedges by [43] (adopted in [44]). We consider infinitely long wedges whose two faces can be made of possibly different materials η_0 and η_1 . Under this model, the field transformation (10) is given as

$$\mathbf{F}_j(\mathbf{E}_j^{\text{In}}(\mathbf{s}_j)) = \mathbf{Q} \mathbf{E}_j^{\text{In}}(\mathbf{s}_j) A^d(\mathbf{s}_{j+1}, \mathbf{s}_j) e^{-j2\frac{\pi}{\lambda}d_{j+1}} \quad (23)$$

where \mathbf{Q} is the diffraction matrix and $A^d(\mathbf{s}_{j+1}, \mathbf{s} + j)$ the spreading factor for diffraction. The computation of \mathbf{Q} is rather involved and requires the computation of Fresnel integrals. However, what matters for the presentation here is that (23) is differentiable with respect to the parameters of the materials of both faces of the wedge. Diffraction is expressed in an edge-fixed coordinate system [41, Sec. 6.2].

F. Path tracing

We consider a fixed maximum number of specular reflections, possibly followed by a diffuse reflection. Only first-order diffraction (i.e., transmitter-diffraction-receiver) is assumed and refraction ignored. Specular paths are found by first determining a set of candidate primitives using shooting-and-bouncing rays (SBR) which are then corrected to exact specular chains using the image method. Diffuse reflections are found through next event estimation in the same process. Candidate edges for diffraction are also identified during SBR and valid points of diffraction are found by the principle of the shortest distance [45]. Note that we do not seek to compute gradients w.r.t. the scene geometry, although this would be in principle possible, e.g., [46]. This has the advantage that the calibration is carried out on the field computations alone which avoids re-tracing of paths for every training iteration.

III. DIFFERENTIABLE RAY TRACING FOR SCENE CALIBRATION

In this section, we will explain how one can parametrize antenna and scattering patterns as well as material properties in a suitable way for gradient-based optimization.

A. Trainable antenna patterns

Antenna patterns as described in Section II-B are square integrable functions on the sphere that need to satisfy the normalization constraint (6). We will now propose a parametric model for a trainable antenna pattern that has these properties. We restrict ourselves to trainable directional gains $G(\theta, \varphi)$ from which the antenna pattern can be computed according to (7). Since many antenna patterns have strong directional characteristics, we model them as a mixture of M spherical Gaussians (or von Mises-Fisher distributions):

$$G(\theta, \varphi) = \eta_{\text{rad}} \sum_{i=1}^M \frac{w_i}{a_i} e^{\lambda_i \boldsymbol{\mu}_i^T \hat{\mathbf{r}}(\theta, \varphi)} \quad (24)$$

$$a_i = \frac{2\pi}{\lambda_i} (e^{\lambda_i} - e^{-\lambda_i}) \quad (25)$$

where $\eta_{\text{rad}} \in [0, 1]$ is the radiation efficiency, $w_i \in [0, 1]$ are mixture weights satisfying $\sum_i w_i = 1$, $\lambda_i > 0$ are concentration parameters, and $\boldsymbol{\mu}_i \in \mathbb{R}^3$ are unit norm mean directions. All of these quantities are modeled as trainable variables.

B. Trainable scattering patterns

In contrast to antenna patterns, scattering patterns are defined on the hemisphere and take three arguments, namely the direction of the incoming and outgoing rays, as well as the

surface normal. Both differences make their parametrization more difficult. We propose the following model which can be considered the hemispherical Gaussian-equivalent to (22) with the addition of a diffuse component:

$$f_s(\hat{\mathbf{k}}_i, \hat{\mathbf{k}}_s, \hat{\mathbf{n}}) = \frac{w_1}{\pi} \hat{\mathbf{k}}_s^T \hat{\mathbf{n}} + \frac{w_2}{a_2} e^{\lambda_2 \hat{\mathbf{k}}_s^T \hat{\mathbf{k}}_i} + \frac{w_3}{a_3} e^{\lambda_3 \hat{\mathbf{k}}_s^T \hat{\mathbf{k}}_r} \quad (26)$$

where $\lambda_2, \lambda_3 \geq 0$ are concentration parameters, $w_i \in [0, 1]$ are mixture weights satisfying $\sum_i w_i = 1$, $\hat{\mathbf{k}}_r = \hat{\mathbf{k}}_i - 2(\hat{\mathbf{n}}^T \hat{\mathbf{k}}_i) \hat{\mathbf{n}}$ is the direction of the specular reflection, and a_i , $i = 2, 3$, are approximate normalization factors given by [47, Algorithm 1]

$$a_i = \frac{2\pi}{\lambda_i} (e^{-\lambda_i} - 1) (2s_i - 1) \quad (27)$$

$$s_i = \frac{e^{t_i} e^{t_i \cos(\beta_i)} - 1}{(e^{t_i} - 1)(e^{t_i \cos(\beta_i)} + 1)} \quad (28)$$

$$t_i = \sqrt{\lambda_i} \frac{1.6988\lambda_i^2 + 10.8438\lambda_i}{\lambda_i^2 + 6.2201\lambda_i + 10.2415} \quad (29)$$

$$\cos(\beta_2) = \hat{\mathbf{k}}_s^T \hat{\mathbf{k}}_i \quad (30)$$

$$\cos(\beta_3) = \hat{\mathbf{k}}_s^T \hat{\mathbf{k}}_r. \quad (31)$$

The difference between the normalization factors a_i in (25) and (27) arises because the integral of the hemispherical Gaussian has no closed-form solution for arbitrary values of $\cos(\beta_i)$. The authors of [47] propose a heuristic approximation which we have used here that achieved excellent accuracy in our experiments, is differentiable, and easy to implement.

C. Trainable materials

As described in Section II-D, a material is characterized by its constituent parameters $\sigma \geq 0$ and $\varepsilon_r \geq 1$, the scattering coefficient $S \in [0, 1]$, and the XPD coefficient $K_x \in [0, 1]$. Although one could immediately consider these parameters as trainable variables, it turned out to be beneficial to use an over-parametrization that helps avoid local minima during gradient-based optimization [48]. We adopt the following model:

$$\sigma = e^{\mathbf{v}^T \mathbf{w}_1} \quad (32)$$

$$\varepsilon_r = 1 + e^{\mathbf{v}^T \mathbf{w}_2} \quad (33)$$

$$S = \text{sigmoid}(\mathbf{v}^T \mathbf{w}_3) \quad (34)$$

$$K_x = \text{sigmoid}(\mathbf{v}^T \mathbf{w}_4) \quad (35)$$

where $\text{sigmoid}(x) = 1/(1 + e^{-x})$, $\mathbf{v} \in \mathbb{R}^L$ and $\mathbf{w}_i \in \mathbb{R}^L$ for $i = 1, \dots, 4$, are trainable vectors in L dimensions. The *read-out vector* \mathbf{v} is used to convert the *embeddings* \mathbf{w}_i to scalar values. As σ and ε_r need to cover a very large range of values, they are represented in the logarithmic domain.

D. Neural materials

The granularity at which material properties in a scene are modeled is an important part of ray tracer calibration. In the simplest case, all objects are made of the same material. One can then subdivide the scene into different object classes with individual materials, e.g., floor, walls, and ceiling. In the most extreme case, all triangles of the meshes defining objects in the scene would have their own materials. This discretization has two difficulties. First, the number of materials that need

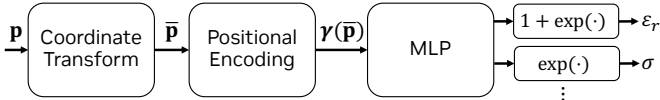


Fig. 1: Processing steps of the computation of neural materials

to be calibrated can become very large. Second, the process of discretizing a scene into objects or parts of objects sharing the same material cannot be easily automated. For this reason, we propose a different approach here called *neural materials* that does not require discretization, is easy to implement and calibrate, and can, in principle, scale to arbitrarily large scenes.

The key idea is to have a small NN, such as a multilayer perceptron (MLP), that computes the corresponding material properties for every ray-scene intersection point. This does not need to be limited to ε_r , σ , S , and K_x , but may also comprise the computation of the weights and concentration parameters of the scattering pattern in (26) among others. Rather than having the NN operate directly on the input coordinates $\mathbf{p} = [x, y, z]^T \in \mathbb{R}^3$, we adopt the positional encoding [49]

$$\gamma(p) = [\sin(2\pi p), \cos(2\pi p), \dots, \sin(2^L \pi p), \cos(2^L \pi p)] \quad (36)$$

that is separately applied to each coordinate. This has been essential to enable NNs to better represent functions with high frequency components over low-dimensional domains [50]. The parameter L controls how fast material properties can vary across space. To make the positional encoding unique, the input coordinates are transformed to the unit cube:

$$\bar{\mathbf{p}} = \frac{\mathbf{p} - \mathbf{b}}{\Delta_b} \quad (37)$$

where $\Delta_b \in \mathbb{R}$ is the length and $\mathbf{b} \in \mathbb{R}^3$ the center of the axis-aligned bounding box (AABB) of the scene, which defines the smallest bounding box that encloses all objects in the scene and has edges parallel to the coordinate axes. The normalized and encoded coordinates $\gamma(\bar{\mathbf{p}}) \in \mathbb{R}^{6L}$ are fed into an MLP which has one output for each parameter. The outputs are then transformed as in (32)–(35). Fig. 1 shows a block diagram of all processing steps. One may also apply the positional encoding on the coordinates represented in the UV space [51] or replace the positional encoding by a multiresolution hash encoding as in [18].

E. Loss function

One challenge related to the calibration of a ray tracer to measurements is the choice of metric or loss function. In our experiments, we have used the following per-example loss

$$\mathcal{L} = l(\tau_{\text{RMS}}, \hat{\tau}_{\text{RMS}}) + l(P, \hat{P}) \quad (38)$$

where

$$l(x, y) = \frac{|x - y|}{x + y} \in [0, 1] \quad (39)$$

is the symmetric mean absolute percentage error (SMAPE),

$$\tau_{\text{RMS}} = \sqrt{\sum_{\ell} \left(\frac{\ell - \bar{\tau}}{W} \right)^2 \frac{p_{\ell}}{P}} \quad (40)$$

is the root mean square (RMS) delay spread with $\bar{\tau} = \sum_{\ell} \ell \frac{p_{\ell}}{P}$ and $p_{\ell} = |h[\ell]|^2$, and P is the total channel gain:

$$P = \sum_{\ell} p_{\ell}. \quad (41)$$

The values \hat{P} and $\hat{\tau}_{\text{RMS}}$ are obtained from ray-traced CIRs, while P and τ_{RMS} are obtained from measurements. The intuition behind the loss in (38) is that the first term measures differences in the delay distribution of the relative path powers while the second term measures differences in the absolute power. As the loss is typically computed over a batch of measurements taken at different positions in a scene, the normalization in (39) ensures that all examples are given equal importance. Without this normalization, the calibration procedure would focus on areas with strong channels, leading to poor performance in areas of weak coverage. The reason why we have chosen this loss over alternatives, such as the power-angular-delay spectrum [28], is that both the RMS delay spread and absolute power are agnostic to time offsets which are present in our dataset. However, alternative losses may be used as drop-in replacements for calibration with other measurements where this is not an issue.

F. Scaling of measurements

A particularity of our channel measurements is that no absolute power reference is known. This means that all examples of the measured dataset are scaled by a common but unknown value $\alpha \in \mathbb{R}$. In order to find a suitable scaling parameter, we estimate it iteratively by an exponentially moving average (EMA) during the calibration process:

$$\alpha_i = \delta \alpha_{i-1} + (1 - \delta) \hat{\alpha}_i, \quad i = 1, 2, \dots \quad (42)$$

where B is the batch size, $\delta > 0$ the decay parameter, $\alpha_0 = \hat{\alpha}_1$, and $\hat{\alpha}_i$ is computed as

$$\hat{\alpha}_i = \arg \min_{\alpha} \frac{1}{B} \sum_{b=1}^B \left(\alpha P_b - \hat{P}_b \right)^2 = \frac{\sum_b P_b \hat{P}_b}{\sum_b P_b^2}. \quad (43)$$

In the limit, α_i is expected to be close to the scaling parameter that solves (43) for the entire dataset. Computing the latter at every iteration would be too costly. In our experiments, this approach has led to better results than learning a scaling factor via gradient descent.

G. Training algorithm

Similar to training an NN, we calibrate our scene using stochastic gradient descent (SGD) on the loss (38) w.r.t. to all trainable parameters of the materials, antenna and scattering patterns described in the previous sections and which we denote by Ω . It is assumed that a reference dataset of D CIRs \mathbf{h}_d together with their associated positions \mathbf{p}_d is available. The algorithm starts by randomly initializing all trainable parameters Ω . It then iteratively computes the scaling factor α_i and the ray tracing predictions $\hat{\mathbf{h}}_b = \text{RT}(\mathbf{p}_b; \Omega)$ for a random batch of B examples and uses the gradient of the average loss over the batch to update the parameters until convergence. Algorithm 1 provides a formal description of this process using

vanilla SGD with a learning rate β for the sake of compactness. Note that any other SGD-variant might be used as well: We employ Adam [31] throughout Section IV.

Algorithm 1: Gradient-based Scene Calibration

Input: B, δ, β
Data: $(\mathbf{h}_d, \mathbf{p}_d)$ for $d \in \mathcal{D} = \{1, \dots, D\}$

- 1 Randomly initialize all trainable parameters Ω
- 2 $i \leftarrow 1$
- 3 **repeat**
- 4 Draw random batch of B examples $\mathcal{B} \subseteq \mathcal{D}$
- 5 Compute α_i as in (42)
- 6 **for** $b \in \mathcal{B}$ **do**
- 7 $\mathbf{h}_b \leftarrow \sqrt{\alpha_i} \mathbf{h}_b$
- 8 $\hat{\mathbf{h}}_b \leftarrow \text{RT}(\mathbf{p}_b; \Omega)$
- 9 Compute sample loss \mathcal{L}_b as in (38)
- 10 **end**
- 11 $\mathcal{L} = \frac{1}{B} \sum_b \mathcal{L}_b$
- 12 $\Omega \leftarrow \Omega - \beta \nabla_{\Omega} \mathcal{L}$
- 13 $i \leftarrow i + 1$
- 14 **until** convergence;

IV. EXPERIMENTS

A. Scenario and measurements

The calibration dataset stems from a small subset of a measurement campaign [34, “dichasus-dc01”] carried out at the Institute of Telecommunications of the University of Stuttgart, utilizing the DICHASUS channel sounder [52]. Instructions about how to access the dataset and 3D scene model can be found in [33]. Measurements were executed at a center frequency of $f = 3.438$ GHz and a signal bandwidth of 50 MHz. CFRs across 1024 OFDM subcarriers were captured at around 32.5k measurement positions from a remote-controlled single-antenna dipole transmitter to two distributed uniform planar 8x4 antenna panels with $\lambda/2$ spacing and vertically polarized antennas. The panels were located at opposing ends of the institute’s hallway (around 50m apart) and the transmitter had its location meticulously tracked using a tachymeter. The data collection was done within the hallway and the entrance hall, as illustrated in Fig. 2. Despite the intricate nature of this setting, characterized by composite walls of drywall, glass, and metal, a ceiling half-covered by a metal grid, and a sizable magnetic board in the entrance hall, we opted for a rudimentary handcrafted 3D model. This model solely represents the visible walls, floor, and ceiling.

B. Synthetic dataset

To validate that scene parameters can be accurately recovered using differentiable ray tracing combined with gradient descent-based optimization, we produced a synthetic dataset using the 3D model of our environment. To make things simple, we considered only a single receive antenna located in the center of the RX 2 panel (see Fig. 2). We then computed CFRs through ray tracing for 256 random transmitter positions, taking into account up to three specular reflections as well

TABLE I: Scene parameters for synthetic dataset generation

Object	ε_r	σ	S	K_x
Floor (ITU Concrete [39])	5.24	0.121	0.3	0.2
Walls (ITU Plasterboard)	2.73	0.027	0.5	0.4
Ceiling (ITU Ceiling board)	1.48	0.004	0.8	0.3

as first-order diffuse scattering and diffraction. All materials were assumed to adhere to the backscattering lobe model with $\alpha_r = 5$, $\alpha_i = 8$, and $\Lambda = 0.8$. Other material parameters are detailed in Table I. In contrast to (19), we did not apply random phase shifts to diffusely reflected paths, i.e., $\chi_1 = \chi_2 = 0$.

We then pretended that the material parameters as well as the scattering and transmit antenna patterns were unknown and tried to recover them by gradient descent on the loss function in (38) using the trainable parametrizations described in Sections III-A–III-C. The material embeddings were chosen to have $L = 30$ dimensions and the transmit antenna pattern $M = 3$ mixtures. It was not necessary to learn a scaling parameter which was set to $\alpha = 1$ (see Section III-F). To speed-up the training process, we separated the path tracing from the field computation. In each training iteration, we computed the field and resulting CFRs for the precomputed geometrical paths and updated all trainable weights based on the loss using the Adam optimizer with a learning rate of 0.01.

Fig. 3 shows learning curves for the four different material parameters of all three objects in the scene. After around 3000 training steps (approx. 10 min on an NVIDIA RTX 3090), all parameters have converged to the correct values. Fig. 4 and Fig. 5 visualize the learned antenna and scattering patterns. Both match the ground truth also very closely. Overall, these results demonstrate that it is possible to recover all scene parameters via gradient descent from an ideal synthetic dataset.

C. Calibration with measured data

Calibrating our ray tracer to the measured dataset faces several challenges. As mentioned in Section III-F, all measured CFRs are scaled by a common but unknown factor α which needs to be estimated. This scaling factor has a very significant impact on the material properties. For example, if the former is too large, the radio environment needs to be overly “reflective” to compensate for the underestimated path loss. Second, no information about absolute path delays is available. For this reason, all measured CIRs are aligned to have the first significant peak on tap $\ell = 0$.

Although we may in principle calibrate antenna and scattering patterns as done for the synthetic dataset, we did not observe any benefits in doing so for our measured dataset. For this reason, diffuse reflections were turned off and the receive and transmit antennas were respectively configured with vertically polarized 3GPP 38.901 [2] and ideal dipole antenna patterns. We have simulated specular reflections up to fifth order as well as first order diffractions. To keep the size of the dataset manageable, we have only used 10k of the available 32.5k measurement points. These were split randomly into 5000 for training, 100 for validation, and 4900 for testing.

The calibration accuracy is quantified as follows. At every measurement point, we compute the average total channel gain

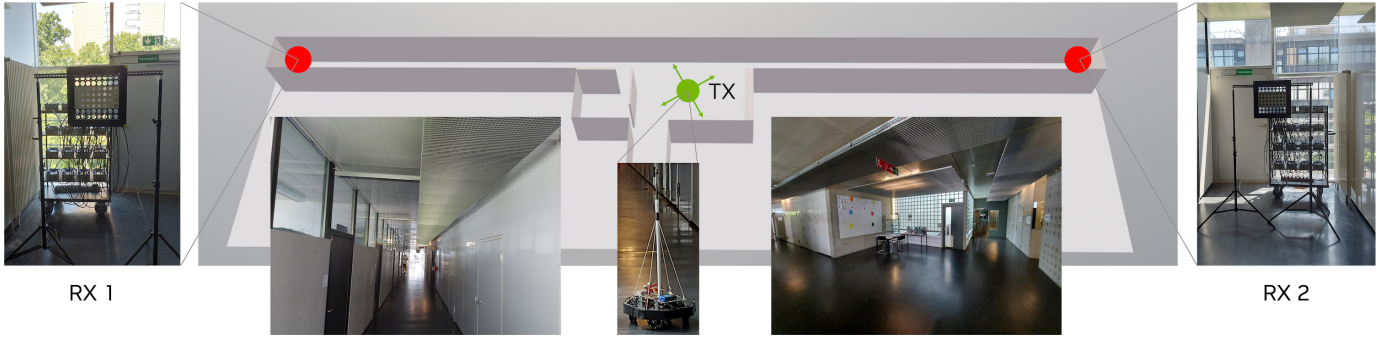


Fig. 2: Measurement setup within the University of Stuttgart’s Institute of Telecommunications. Two 32-antenna panels from the DICHASUS channel sounder were positioned at opposing ends of the main corridor. A remotely-operated transmitter navigated the hallway and entrance hall along a pseudo-random path.

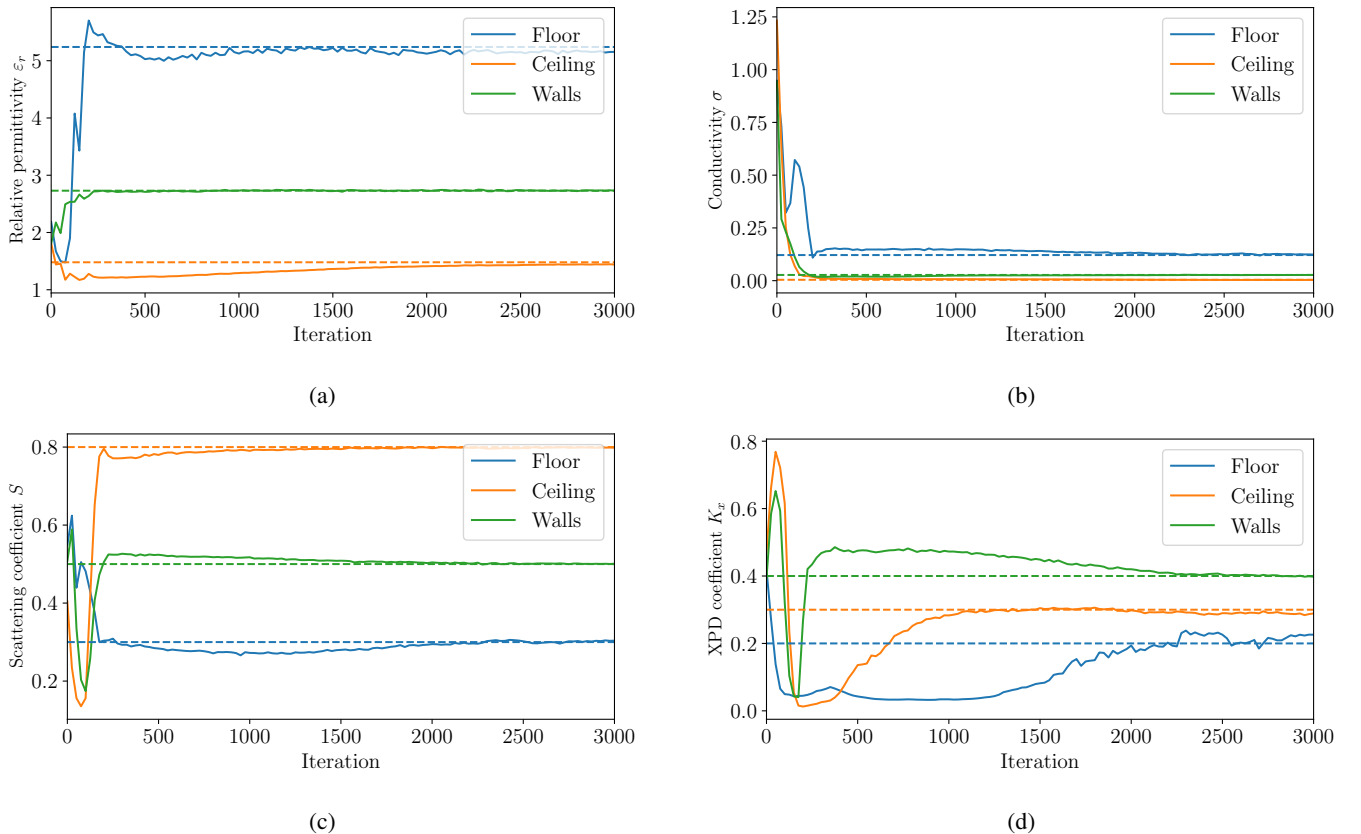


Fig. 3: Learning curves for the material parameters of all objects in the scene. Dashed and solid lines represent ground truth and learned values, respectively. All parameters can be almost perfectly recovered within 3000 iterations.

P (41) and RMS delay spread τ_{RMS} (40) over the CIRs from the transmitter to all 64 receive antennas across the two arrays. These quantities are denoted by \bar{P} , $\bar{\tau}_{\text{RMS}}$ and \hat{P} , $\hat{\tau}_{\text{RMS}}$ for the measured and ray-traced CIRs, respectively. We then compute the absolute logarithmic error (ALE) for the channel gain:

$$\text{ALE} = |\bar{P}_{\text{dB}} - \hat{P}_{\text{dB}}| \quad (44)$$

and the relative absolute error (RAE) for the delay spread:

$$\text{RAE} = \frac{|\bar{\tau}_{\text{RMS}} - \hat{\tau}_{\text{RMS}}|}{\bar{\tau}_{\text{RMS}}}. \quad (45)$$

In the following, we will show results for an uncalibrated baseline as well as two different calibration techniques. For the baseline that will be referred to as “ITU Materials”, the scene is configured as described in Table I with $S = K_x = 0$. The first calibration technique is named “Learned Materials” and refers to the parametrization described in Section III-C with material embeddings of $L = 30$ dimensions. The second, called “Neural Materials”, is based on the approach described in Section III-D with a positional encoding of size $L = 10$ and an MLP consisting of four hidden layers with 128 neurons each and rectified linear unit (ReLU) activations.

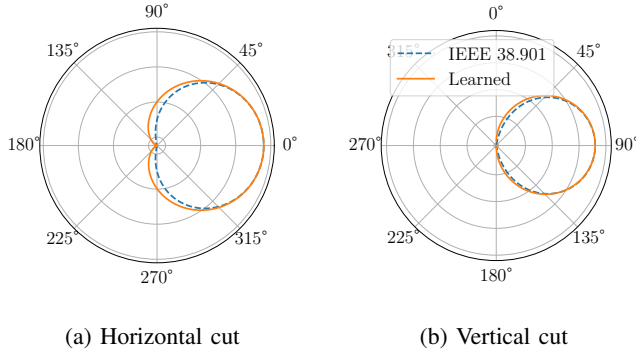


Fig. 4: Visualization of the learned antenna pattern

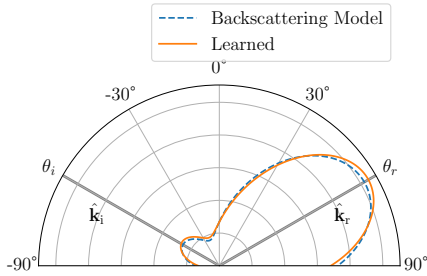


Fig. 5: Visualization of the learned backscattering pattern. The quantities θ_i and θ_r denote the angles of the incident and specular directions with the surface normal, respectively.

The top row of Fig. 6 shows a heatmap of the path loss $-P_{\text{dB}}$, i.e., the inverse total channel gain, for the measurements, the “ITU Materials”, as well as both calibration techniques for RX 2, located in the right wing. The bottom row shows the associated ALE. One can clearly see the benefits of “Learned Materials” in the left corridor where the ALE is substantially improved w.r.t. to the “ITU Materials”. However, due to the overly simplistic scene modelling, large errors in the entrance hall persist even after calibration. The “Neural Materials” show uniformly improved performance across the whole area. Fig. 7a provides another look at these results via the cumulative distribution function (CDF) of the ALE. “Neural Materials” not only achieve superior accuracy for the path loss, but also the delay spread which can be seen from the CDF of the RAE in Fig. 7b. The corresponding error statistics are provided in Table II

Fig. 8 depicts measured and simulated CIRs at four different positions. The “ITU Materials” generally fail to model paths with long propagation delays which can be partially compensated for through calibration using “Learned Materials” (cf.

TABLE II: Error statistics

Metric	ALE (power)		RAE (delay spread)	
Statistic	mean	std	mean	std
ITU Materials	4.93	5.26	0.54	0.23
Learned Materials	2.16	1.69	0.24	0.17
Neural Materials	1.00	0.95	0.13	0.12

Fig. 7b). However, due to the very coarse scene representation, this impacts the accuracy of early reflections. The fine-grained modeling capabilities of “Neural Materials” do not suffer from this problem and are capable of producing CIRs that closely resemble the measurements.

Fig. 9 illustrates the reflection coefficient $r = \frac{1}{2}(|r_{\perp}|^2 + |r_{\parallel}|^2)$ at an incident angle of $\theta_i = 45^\circ$; comparing “Learned-” and “Neural Materials” across the scene. The “Neural Materials” notably assign high values to the locations of the metallic grid on the ceiling and the magnetic board on a wall in the entrance hall, as seen in Fig. 2. While further study is needed, these observations suggest that “Neural Materials” can effectively represent objects’ electromagnetic behaviors in a scene, offering a unique perspective on the environment through the lens of radio propagation.

D. Discussion

We have only scratched the surface of gradient-based calibration in this paper and many open questions remain to be answered. We will now briefly discuss a few of them:

- The loss function (38) is non-convex in the scene parameters and there is no guarantee that gradient-based solutions will converge to the global minimum. It is not even clear if there is a unique optimal solution. For example, the same absolute value of a reflection coefficient (17) can be obtained for different values of conductivity and permittivity. Regularization of parameters during calibration may enforce plausible solutions.
- Although all parameters have clear physical interpretations, the calibration does not necessarily lead to the same values which would be obtained by directly measuring them for each object. The reason for this is that calibration also compensates for errors in the geometry and measurements as well as modelling errors in the RT process. For example, we have entirely ignored refraction in Section IV-C, which certainly plays an important role in our indoor scenario.
- The advantage of “Neural Materials” is their capability to represent material properties in a very fine-grained (continuous) manner across the entire scene. However, this comes at the cost of poor generalization performance to areas in which no measurements are available. Investigating their bias-variance trade-off is an important topic of future research. It is also interesting to study extensions or alternatives to the positional encoding (36).
- Our calibration method is agnostic to phase errors. One may learn location-specific phase correction terms through “Neural Materials” or investigate phase-error aware calibration techniques.

V. CONCLUSIONS

In this paper, we have introduced a novel gradient-based calibration method for differentiable ray tracers, enabling scene calibration akin to training a deep neural network. This method hinges on a carefully designed loss function, coupled with differentiable parameterizations of material properties, scattering

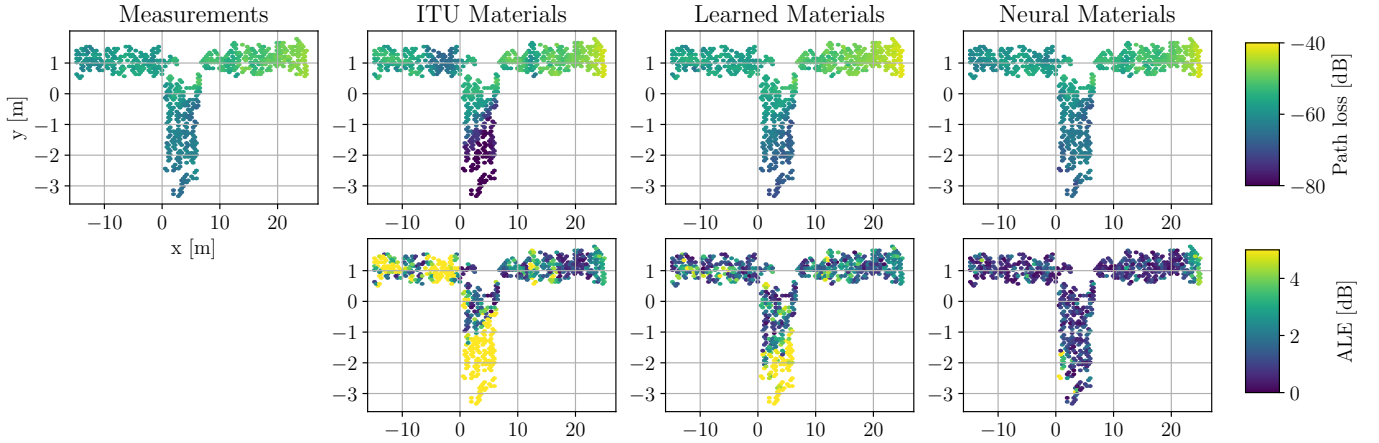
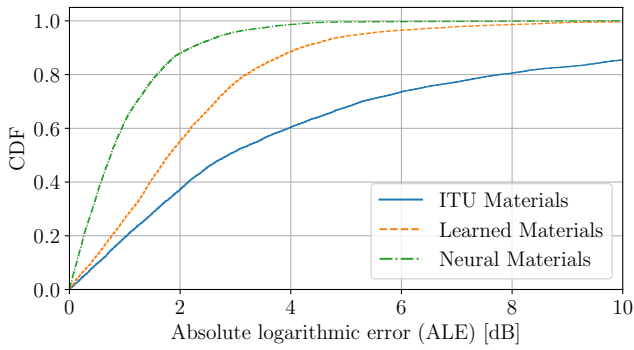
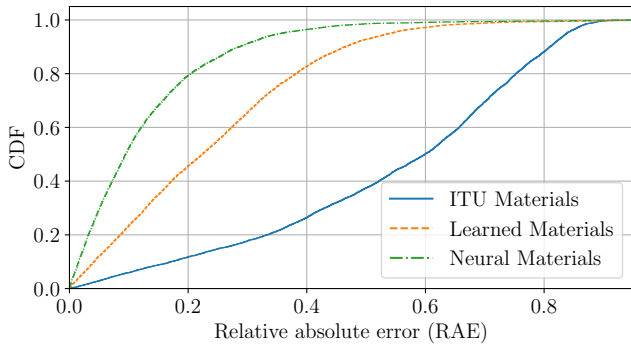


Fig. 6: Visualization of path loss ($-P_{dB}$) and absolute logarithmic error (ALE) across space for different calibration techniques



(a) Channel gain



(b) Delay spread

Fig. 7: CDFs of the ALE and RAE

behaviors, and antenna patterns. We have implemented our calibration method in the open-source ray tracer Sionna RT [30] and validated it against indoor measurements from a distributed multiple-input multiple-output (MIMO) channel sounder. This advancement in differentiable ray tracing, especially when combined with contemporary machine learning techniques, opens up exciting avenues for multidisciplinary research and holds immense potential for future explorations.

REFERENCES

- [1] Z. Yun and M. F. Iskander, "Ray tracing for radio propagation modeling: Principles and applications," *IEEE Access*, vol. 3, Jul. 2015.
- [2] "TR 38.901: Study on channel model for frequencies from 0.5 to 100 GHz," 3GPP, Tech. Rep. 17.0.0, Mar. 2022.
- [3] A. Bourdoux, A. N. Barreto, B. van Liempd, C. de Lima, D. Dardari, D. Belot, E.-S. Lohan, G. Seco-Granados, H. Sariyedeen, H. Wymeersch, J. Suutala, J. Saloranta, M. Guillaud, M. Isomursu, M. Valkama, M. R. K. Aziz, R. Berkvens, T. Sanguanpuak, T. Svensson, and Y. Miao, "6G White Paper on Localization and Sensing," *University of Oulu: 6G Research Visions*, Jun. 2020.
- [4] A. Alkhateeb, G. Charan, T. Osman, A. Hredzak, J. Morais, U. Demirhan, and N. Srinivas, "DeepSense 6G: A large-scale real-world multi-modal sensing and communication dataset," *arXiv preprint arXiv:2211.09769*, 2022.
- [5] M. D. Renzo, M. Debbah, D.-T. Phan-Huy, A. Zappone, M.-S. Alouini, C. Yuen, V. Sciancalepore, G. C. Alexandropoulos, J. Hoydis, H. Gacanin, J. d. Rosny, A. Bounceur, G. Lerosey, and M. Fink, "Smart radio environments empowered by reconfigurable AI meta-surfaces: An idea whose time has come," vol. 2019, no. 1, p. 129, May 2019.
- [6] C. Studer, S. Medjkouh, E. Gonultaş, T. Goldstein, and O. Tirkkonen, "Channel charting: Locating users within the radio environment using channel state information," *IEEE Access*, vol. 6, pp. 47 682–47 698, 2018.
- [7] J. Hoydis, F. A. Aoudia, A. Valcarce, and H. Viswanathan, "Toward a 6G AI-Native Air Interface," *IEEE Commun. Mag.*, vol. 59, no. 5, pp. 76–81, May 2021.
- [8] RP-212708, "New SID on AI/ML for NR Air Interface," 3GPP TSG RAN#94e, Tech. Rep., Dec. 2021.
- [9] A. Alkhateeb, S. Jiang, and G. Charan, "Real-Time Digital Twins: Vision and Research Directions for 6G and Beyond," *arXiv e-prints*, pp. arXiv-2301, 2023.
- [10] X. Lin, L. Kundu, C. Dick, E. Obiodu, and T. Mostak, "6G Digital Twin Networks: From Theory to Practice," *arXiv preprint arXiv:2212.02032*, 2022.
- [11] S. Bakirtzis, K. Qiu, J. Zhang, and I. Wassell, "DeepRay: Deep Learning Meets Ray-Tracing," in *16th European Conf. Ant. Prop. (EuCAP)*, Madrid, Spain, Mar. 2022, pp. 1–5.
- [12] L. Azpilicueta, M. Rawat, K. Rawat, F. M. Ghannouchi, and F. Falcone, "A ray launching-neural network approach for radio wave propagation analysis in complex indoor environments," *IEEE Trans. Antennas Propag.*, vol. 62, no. 5, pp. 2777–2786, Feb. 2014.
- [13] X. Zhang, X. Shu, B. Zhang, J. Ren, L. Zhou, and X. Chen, "Cellular network radio propagation modeling with deep convolutional neural networks," in *Proc. 26th ACM SIGKDD Int. Conf. Knowledge discovery & Data Mining*, Aug. 2020, pp. 2378–2386.
- [14] R. Levie, C. Yapar, G. Kutyniok, and G. Caire, "RadioUNet: Fast Radio Map Estimation With Convolutional Neural Networks," *IEEE Trans. Wireless Commun.*, vol. 20, no. 6, pp. 4001–4015, Feb. 2021.
- [15] L. Eller, P. Svoboda, and M. Rupp, "A Deep Learning Network Planner: Propagation Modeling Using Real-World Measurements and a 3D City Model," *IEEE Access*, vol. 10, pp. 122 182–122 196, Nov. 2022.

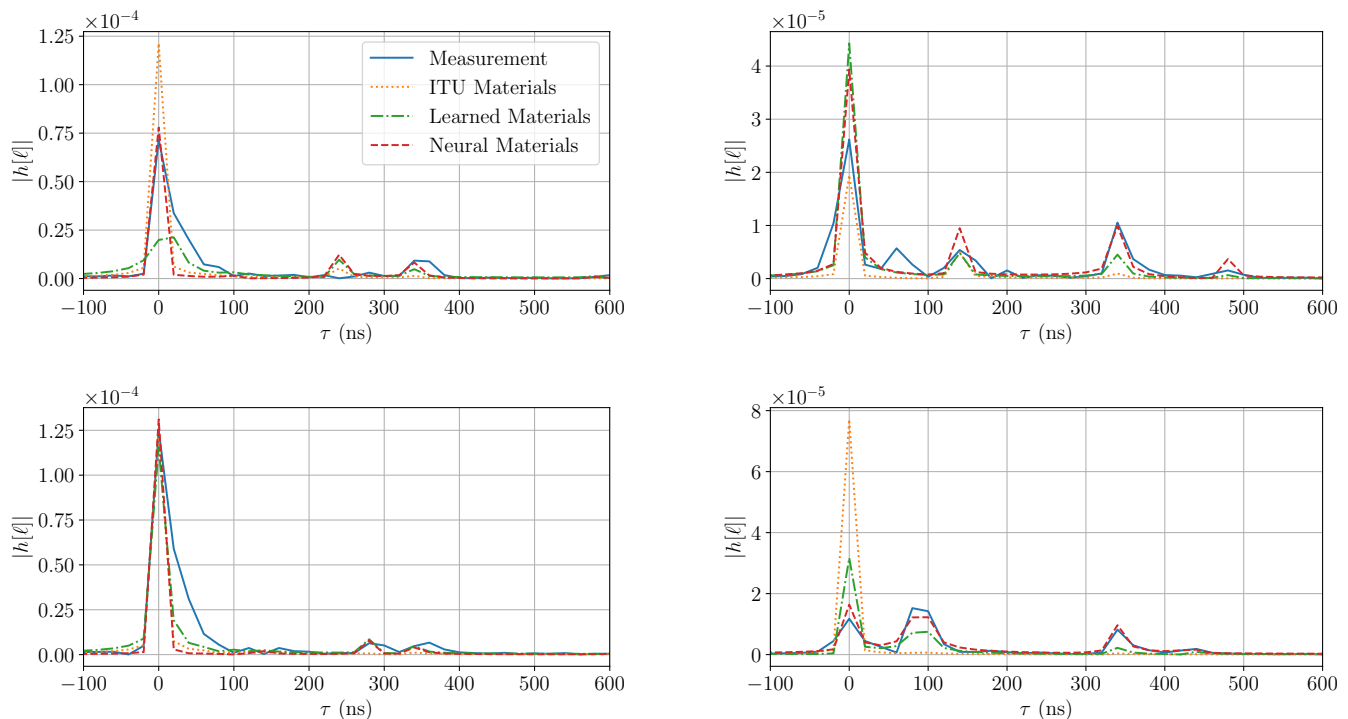


Fig. 8: CIR examples for different measurement positions and calibration techniques

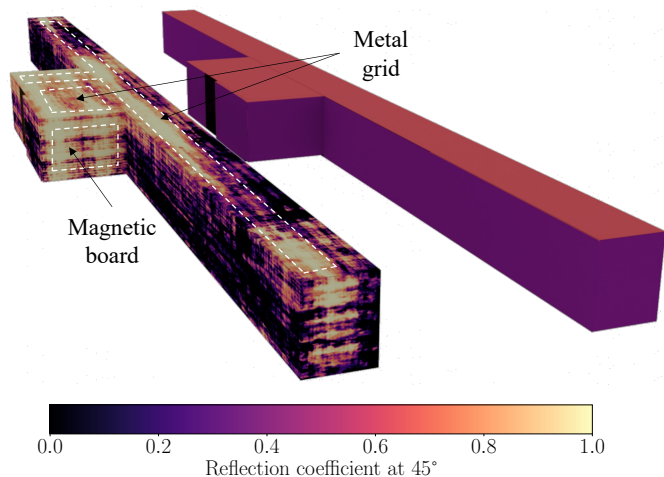


Fig. 9: Visualization of the reflection coefficient across the scene: Neural Materials (left), Learned Materials (right).

- [16] A. Gupta, J. Du, D. Chizhik, R. A. Valenzuela, and M. Sellathurai, "Machine Learning-Based Urban Canyon Path Loss Prediction Using 28 GHz Manhattan Measurements," *IEEE Trans. Antennas Propag.*, vol. 70, no. 6, pp. 4096–4111, Feb. 2022.
- [17] T. Orekondy, P. Kumar, S. Kadambi, H. Ye, J. Soriaga, and A. Behboodi, "WiNeRT: Towards neural ray tracing for wireless channel modelling and differentiable simulations," in *International Conference on Learning Representations*, 2023.
- [18] T. Müller, A. Evans, C. Schied, and A. Keller, "Instant neural graphics primitives with a multiresolution hash encoding," *ACM Trans. Graph.*, vol. 41, no. 4, pp. 102:1–102:15, Jul. 2022.
- [19] T.-M. Li, M. Aittala, F. Durand, and J. Lehtinen, "Differentiable Monte Carlo ray tracing through edge sampling," *ACM Trans. Graph.*, vol. 37, no. 6, Dec. 2018.
- [20] W. Jakob, S. Speierer, N. Roussel, and D. Vicini, "Dr.Jit: A just-in-time compiler for differentiable rendering," *Transactions on Graphics (Proceedings of SIGGRAPH)*, vol. 41, no. 4, Jul. 2022.
- [21] W. Jakob, S. Speierer, N. Roussel, M. Nimier-David, D. Vicini, T. Zeltner, B. Nicolet, M. Crespo, V. Leroy, and Z. Zhang, "Mitsuba 3 Renderer," 2022, <https://mitsuba-renderer.org>.
- [22] Z. Li, T. Müller, A. Evans, R. H. Taylor, M. Unberath, M.-Y. Liu, and C.-H. Lin, "Neuralangelo: High-fidelity neural surface reconstruction," in *IEEE Conf. Computer Vision and Pattern Recognition (CVPR)*, 2023.
- [23] K. Guan, B. Ai, B. Peng, D. He, G. Li, J. Yang, Z. Zhong, and T. Kürner, "Towards realistic high-speed train channels at 5G millimeter-wave band—Part I: Paradigm, significance analysis, and scenario reconstruction," *IEEE Trans. Veh. Technol.*, vol. 67, no. 10, pp. 9112–9128, Oct. 2018.
- [24] O. Kanhere and T. S. Rappaport, "Calibration of NYURay, a 3D mmWave and sub-THz ray tracer using indoor, outdoor, and factory channel measurements," *arXiv preprint arXiv:2302.12380*, Feb. 2023.
- [25] J. Jemai, P. C. Eggers, G. F. Pedersen, and T. Kurner, "Calibration of a UWB sub-band channel model using simulated annealing," *IEEE Trans. Antennas Propag.*, vol. 57, no. 10, pp. 3439–3443, Oct. 2009.
- [26] M. Gan, P. Meissner, F. Mani, E. Leitinger, M. Fröhle, C. Oestges, K. Witrisal, and T. Zemen, "Calibration of indoor UWB sub-band divided ray tracing using multiobjective simulated annealing," in *IEEE Int. Conf. Commun. (ICC)*, Sydney, NSW, Australia, Jun. 2014, pp. 4844–4849.
- [27] D. He, B. Ai, K. Guan, Z. Zhong, B. Hui, J. Kim, H. Chung, and I. Kim, "Channel measurement, simulation, and analysis for high-speed railway communications in 5G millimeter-wave band," *IEEE Trans. Intell. Transp. Syst.*, vol. 19, no. 10, pp. 3144–3158, Oct. 2018.
- [28] R. Charbonnier, C. Lai, T. Tenoux, D. Caudill, G. Gougeon, J. Senic, C. Gentile, Y. Corre, J. Chuang, and N. Gollmie, "Calibration of ray-tracing with diffuse scattering against 28-GHz directional urban channel measurements," *IEEE Trans. Veh. Technol.*, vol. 69, no. 12, pp. 14264–14276, Oct. 2020.
- [29] G. S. Bhatia, Y. Corre, and M. Di Renzo, "Tuning of ray-based channel model for 5G indoor industrial scenarios," in *IEEE Int. Mediterranean Conf. Commun. Network. (MeditCom)*, Dubrovnik, Croatia, Sep. 2023, pp. 311–316.
- [30] J. Hoydis, F. Ait Aoudia, S. Cammerer, M. Nimier-David, N. Binder, G. Marcus, and A. Keller, "Sionna RT: Differentiable Ray Tracing for Radio Propagation Modeling," *arXiv preprint*, Mar. 2023.

- [31] D. P. Kingma and J. Ba, "Adam: A method for stochastic optimization," *arXiv preprint arXiv:1412.6980*, 2014.
- [32] M. Raissi, P. Perdikaris, and G. E. Karniadakis, "Physics-informed neural networks: A deep learning framework for solving forward and inverse problems involving nonlinear partial differential equations," *Journal of Computational physics*, vol. 378, pp. 686–707, 2019.
- [33] J. Hoydis, F. Ait Aoudia, S. Cammerer, M. Nimier-David, and A. Keller, "Learning radio environments by differentiable ray tracing," Dec. 2023. [Online]. Available: <https://github.com/NVlabs/diff-rt-calibration>
- [34] F. Euchner, P. Stephan, M. Gauger, and S. ten Brink, "dichasus-dcxx: Institute hallway with known 3D model, distributed antennas," <https://dichasus.inue.uni-stuttgart.de/datasets/data/dichasus-dcxx/>, Dec. 2023.
- [35] T. Fugen, J. Maurer, T. Kayser, and W. Wiesbeck, "Capability of 3-D ray tracing for defining parameter sets for the specification of future mobile communications systems," *IEEE Trans. Antennas Propag.*, vol. 54, no. 11, pp. 3125–3137, Nov. 2006.
- [36] C. A. Balanis, *Antenna Theory: Analysis and Design*, 2nd ed. John Wiley & Sons, 1997.
- [37] V. Degli-Esposti, F. Fuschini, E. M. Vitucci, and G. Falciasecca, "Measurement and modelling of scattering from buildings," *IEEE Trans. Antennas Propag.*, vol. 55, no. 1, pp. 143–153, Jan. 2007.
- [38] V. Degli-Esposti, V.-M. Kolmonen, E. M. Vitucci, and P. Vainikainen, "Analysis and modeling on co-and cross-polarized urban radio propagation for dual-polarized MIMO wireless systems," *IEEE Trans. Antennas Propag.*, vol. 59, no. 11, pp. 4247–4256, Aug. 2011.
- [39] ITU, "Recommendation ITU-R P.2040-3: Effects of building materials and structures on radiowave propagation above about 100 MHz," Tech. Rep., Aug. 2023.
- [40] G. A. Deschamps, "Ray techniques in electromagnetics," *Proc. IEEE*, vol. 60, no. 9, pp. 1022–1035, Sep. 1972.
- [41] D. A. McNamara, C. W. I. Pistorius, and J. A. G. Malherbe, *Introduction to the uniform geometrical theory of diffraction*. Artech House, 1990.
- [42] R. G. Kouyoumjian and P. H. Pathak, "A uniform geometrical theory of diffraction for an edge in a perfectly conducting surface," *Proc. IEEE*, vol. 62, no. 11, pp. 1448–1461, Nov. 1974.
- [43] R. Luebbers, "Finite conductivity uniform GTD versus knife edge diffraction in prediction of propagation path loss," *IEEE Trans. Antennas Propag.*, vol. 32, no. 1, pp. 70–76, Jan. 1984.
- [44] ITU, "Recommendation ITU-R P.526-15: Propagation by diffraction," Tech. Rep., Oct. 2019.
- [45] J. B. Keller, "Geometrical theory of diffraction," *Journal of the Optical Society of America*, vol. 52, no. 2, pp. 116–130, Feb. 1962.
- [46] B. Nicolet, A. Jacobson, and W. Jakob, "Large steps in inverse rendering of geometry," *ACM Trans. Graph.*, vol. 40, no. 6, dec 2021.
- [47] J. Meder and B. Bröderlin, "Hemispherical Gaussians for accurate light integration," in *Proc. Int. Conf. Computer Vision and Graphics (ICCVG)*, Warsaw, Poland, Sep. 2018, pp. 3–15.
- [48] A. Choromanska, M. Henaff, M. Mathieu, G. Ben Arous, and Y. LeCun, "The loss surfaces of multilayer networks," in *Proc. Int. Conf. Artificial Intelligence and Statistics (PMLR)*, vol. 38, San Diego, California, USA, 9–12 May 2015, pp. 192–204.
- [49] B. Mildenhall, P. P. Srinivasan, M. Tancik, J. T. Barron, R. Ramamoorthi, and R. Ng, "NeRF: Representing scenes as neural radiance fields for view synthesis," *Communications of the ACM*, vol. 65, no. 1, pp. 99–106, Jan. 2021.
- [50] M. Tancik, P. Srinivasan, B. Mildenhall, S. Fridovich-Keil, N. Raghavan, U. Singhal, R. Ramamoorthi, J. Barron, and R. Ng, "Fourier features let networks learn high frequency functions in low dimensional domains," in *Advances in Neural Information Processing Systems*, H. Larochelle, M. Ranzato, R. Hadsell, M. Balcan, and H. Lin, Eds., vol. 33. Curran Associates, Inc., Aug. 2020, pp. 7537–7547.
- [51] M. Pharr, W. Jakob, and G. Humphreys, *Physically Based Rendering: From Theory to Implementation*, 4th ed. MIT Press, 2023.
- [52] F. Euchner, M. Gauger, S. Dörner, and S. ten Brink, "A distributed massive MIMO channel sounder for "Big CSI Data"-driven machine learning," in *Int. ITG Workshop Smart Antennas (WSA)*, Sophia-Antipolis, France, Nov. 2021.